

ExPRES: a Tool to Simulate Exoplanetary and Planetary Radio Emissions

C. K. Louis^{1,2,3}, S. L. G. Hess⁴, B. Cecconi^{2,3}, P. Zarka^{2,3}, L. Lamy^{2,3}, S. Aicardi⁵, and A. Loh²

¹ Institut de Recherche en Astrophysique et Planétologie (IRAP), CNRS, Université Paul Sabatier, Toulouse, France
e-mail: corentin.louis@irap.omp.eu

² LESIA, Observatoire de Paris, PSL Research University, CNRS, Sorbonne Universités, UPMC Univ. Paris 06, Univ. Paris Diderot, Sorbonne Paris Cité, Meudon, France

³ USN, Observatoire de Paris, CNRS, PSL, UO/OSUC, Nançay, France

⁴ ONERA-The French Aerospace Lab, FR-31055 Toulouse, France

⁵ DIO, Observatoire de Paris, PSL Research University, CNRS, Paris, France

ABSTRACT

Context. All magnetized planets are known to produce intense non-thermal radio emissions through a mechanism known as Cyclotron Maser Instability (CMI), requiring the presence of accelerated electrons generally arising from magnetospheric current systems. In return, radio emissions are a good probe of these current systems and acceleration processes. The CMI generates highly anisotropic emissions and leads to important visibility effects, which have to be taken into account when interpreting the data. Several studies showed that modeling the radio source anisotropic beaming pattern can reveal a wealth of physical information about the planetary or exoplanetary magnetospheres that produce these emissions.

Aims. We present a numerical tool, called ExPRES (Exoplanetary and Planetary Radio Emission Simulator), which is able to reproduce the occurrence in time-frequency plane of CMI-generated radio emissions from planetary magnetospheres, exoplanets or star-planet interacting systems. Special attention is given to the computation of the radio emission beaming at and near its source.

Methods. We explain what physical information about the system can be drawn from such radio observations, and how it is obtained. These information may include the location and dynamics of the radio sources, the type of current system leading to electron acceleration and their energy and, for exoplanetary systems, the magnetic field strength, the orbital period of the emitting body and the rotation period, tilt and offset of the planetary magnetic field. Most of these parameters can be remotely measured only via radio observations.

Results. The ExPRES code provides the proper framework of analysis and interpretation for past (Cassini, Voyager, Galileo...), current (*Juno*, ground-based radiotelescopes) and future (BepiColombo, Juice) observations of planetary radio emissions, as well as for future detection of radio emissions from exoplanetary systems (or magnetic white dwarf-planet or white dwarf-brown dwarf systems). Our methodology can be easily adapted to simulate specific observations, once effective detection is achieved.

Key words. Planets and satellites: Aurorae — Radio continuum: Planetary systems — Planet-star interactions — Radio emissions simulation

1. Introduction

1.1. Planetary radio emissions

All planets in our solar system that possess an internal magnetic field are known to emit low frequency radio emissions, in wavelength domains extending from kilometer (below ~ 100 kHz) up to decameter (a few tens of MHz — in the case of Jupiter only). The frequency domain corresponds to the electron cyclotron frequencies (f_{ce}) close to the planet, revealing that the emission process is related to the electron gyration along the planet's magnetic field lines. Theoretical work and in situ observations of the terrestrial, kronian and jovian radio sources permitted to elucidate the physical process at the origin of the radio emissions: the Cyclotron-Maser Instability (CMI), which occurs when an elliptically polarized wave resonates with the gyration motion of accelerated electrons (see Wu 1985; Louarn 1992; Zarka 1998; Treumann 2006; Louarn et al. 2017; Lamy et al. 2018). Under some circumstances — notably a positive gradient of the perpendicular velocity distribution of the electrons — the CMI mainly amplifies the wave on the extraordinary mode which can escape the source and propagate in free space as a radio wave.

The interest for planetary low-frequency radio emissions is driven by their relation with accelerated electrons. Those are also responsible for auroral emissions on top of the planet's atmosphere (over a broad spectral domains extending from Infrared to X-rays) and reveal the presence of field-aligned currents coupling the magnetosphere to the planet's ionosphere. Contrary to the other auroral emissions, radio emissions are not emitted on top of the planet's atmosphere but along a larger altitude range extending from the top of the ionosphere up to a few planet radii (see review by Zarka 1998). The emission frequency is close to f_{ce} in the source, itself proportional to the local magnetic field strength which decreases with increase altitude. Hence, the radio source altitude can be deduced from the frequency at which it emits. This property can be used to probe large altitude ranges above the auroras and to reveal, for example, the presence of acceleration regions (Pottellette & Pickett 2007; Hess et al. 2007b, 2010a).

1.2. Visibility and variability of the sources

The CMI is very sensitive to the plasma characteristics in the source, such as the density and temperature of the different electron populations, and the shape of the electron velocity distribution (Pritchett 1984; Louarn & Le Quéau 1996b). These parameters not only condition and affect the amplification and the propagation of the wave, but they also have a huge impact on the beaming pattern of the emission (see section 3.3). Typical CMI emissions are radiated on a few degrees (Kaiser et al. 2000; Zarka 2004) of a given angle relative to the magnetic field. By symmetry around the magnetic field direction, the emission pattern is a thin hollow cone. This strong anisotropy of the radio emission beaming has two consequences regarding the observations of planetary auroral radio emission: (1) the observations have to be detrended from the source visibility effects before being interpreted — no detection of the emission does not mean that no emission is produced —, and (2) as the beaming pattern strongly depends on the plasma characteristics close to the source, the visibility of the emissions carries information about the plasma parameters at the source.

Visibility effects are responsible for the ubiquitous arc shapes of the radio emission patterns in the time-frequency plane, as illustrated by the examples of jovian and kronian emissions displayed on Figure 1. Panels 1a and 1b respectively show typical emissions from Jupiter (Queinnec & Zarka 1998) and from Saturn (including arcs generated by hot-spots in sub-rotation in Saturn’s magnetosphere, Lamy et al. 2008, 2013). The arc shape is a direct consequence of the hollow cone beaming pattern of the source, as shown on Panels 1c–e in the simple case of a dipolar-axisymmetric magnetic field. The radio emission from a radiating field line is received once when the source is on the western side of the observer’s meridian (i.e., before the meridian relative to the sense of planetary rotation) and that one side of the cone is directed toward the observer. It is observed again when the field line is on the eastern side of the meridian and that the other side of the cone is directed toward the observer. As a result, for a fixed observer and a field line moving in the sense of rotation, radio emission at a given frequency can thus be observed twice, once or none depending on the geometry of the beaming pattern.

To interpret observations of planetary auroral radio emission, it is thus necessary to take into account their beaming pattern for inferring the effect of the visibility of the source. Some studies assumed constant beaming angles along the field lines (Genova & Aubier 1985; Lecacheux et al. 1998), while others allowed the beaming angle to vary with the frequency (Queinnec & Zarka 1998; Hess et al. 2014), in order to determine the source location. For some case studies, e.g. of specific radio arcs, a beaming pattern can be deduced from the observed arc shape assuming a source location (or possible source locations), as in Queinnec & Zarka (1998), or using the source location provided by an independent method such as radio goniopolarimetry (Ceconi et al. 2009; Lamy et al. 2011). Deriving physical source parameters directly from observations can be qualified of ‘inverse modeling’. It allows to infer source and emission parameters that are consistent with a given observation of a radio arc, but it does not prove that only the observed arc should indeed be visible at the time of observation, i.e., it does not entirely de-trend the observation from the beaming effect. Moreover, the inverse modeling often implies to determine both the position and the beaming pattern from a single observation, whereas these two parameters are strongly coupled leading to degeneracy of the solution (Hess et al. 2010a). For a more global interpretation of radio dynamic

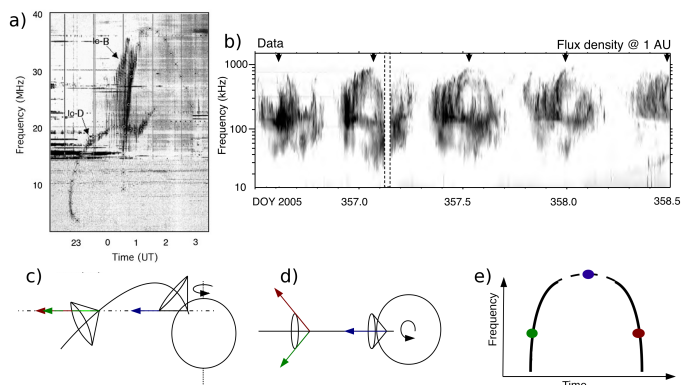


Fig. 1. a-b) Examples of time-frequency radio arcs. a) Radio arcs emitted by the Io-Jupiter interaction (Queinnec & Zarka 1998), observed by Wind (0–15 MHz) and the Nanç Decameter Array (15–40 MHz). b) Radio arcs at Saturn, observed by Cassini, related to a sub-rotating hot spot in Saturn’s magnetosphere (Lamy et al. 2008). c) and d) Side and polar views of the emission geometry, with two sources located along the same magnetic field line but at different altitudes. Arrows show the direction of propagation of the radio waves which can be seen by an observer located in the equatorial plane far from the planet. e) Dynamic spectrum of the emissions which would correspond to the above geometry.

spectra, a ‘forward modeling’ approach may be better: it consists of assuming source and emission parameters for computing a predicted dynamic spectrum, that is then compared to the observations. Matching of the predicted and observed dynamic spectra is a strong proof of the adequacy of the model to the reality of the source parameters and emission process. Of course, good matches may be obtained for non unique sets of parameters. Nevertheless, modeling of various observations corresponding to different viewing geometries is expected to remove this degeneracy and permit to better constrain the source conditions.

1.3. Visibility modeling

Implementing this forward modeling approach is the purpose of the numerical code described in the present paper, the Exoplanetary and Planetary Radio Emission Simulator (ExPRES). This code uses as inputs the geometry of the observation (observer and celestial bodies positions, sources location and magnetic field topology), the plasma parameters in the sources and their vicinity (density and temperature) as well as the characteristics of the wave-particle interaction generating the radio emissions constrained by the CMI theory. From these inputs, the code computes the beaming pattern of the radio sources, compares the direction of emissions to the direction of the observer and generates time-frequency visibility maps, that can be directly compared to observed dynamic spectra (Section 2).

In the following, we summarize the physics of planetary auroral radio emissions and how it is taken into account in ExPRES, starting with of the magnetospheric interactions powering the emissions and their impact on the CMI (Section 3). We then more specifically discuss the radio emission beaming (Section 4). We show that the different cases of auroral radio emission observed in our solar system can be described using a small number of parameters, which define both the location of the sources and their beaming pattern. Finally we describe the outputs parameters of the code, show some simulations examples and list simulations results already obtained with ExPRES (Section 5).

2. ExPRES modeling

The computation of a synthetic dynamic spectrum with ExPRES mostly relies on the observation geometry. An example is shown on Figure 2, which sketches the geometry of the observation of emissions triggered by the Io-Jupiter interaction. For a given source-observer geometry (relative positions of the source and the observer at a given time and for a given emission frequency), magnetic field orientation in the source (depending on a magnetic field model), and beaming pattern (depending on electron densities and energies at the source, as discussed in Section 4), the code compares the direction of beamed RX mode waves with the source-to-observer direction. If the angle between these directions is smaller than the beam width, defined by the user, the corresponding time-frequency pixel in the synthetic dynamic spectrum is incremented by 1, otherwise it is not. By repeating this computation at all time-frequency steps of interest, for all elementary point sources constituting the user-defined radio source, a visibility map is generated in the time-frequency plane. ExPRES counts by default a standard intensity value of 1 (unit-less) for each radio source. More physical intensities can nonetheless be used to achieve realistic simulations (see example in Lamy et al. 2013).

The set of parameters that the user needs to feed ExPRES with in order to perform a simulation run is:

- The definition of the celestial bodies involved in the simulation (star, planet, satellite), with their respective positions at each time step (pre-computed or deduced from initial positions and orbital parameters), their rotation / revolution period, and their size and mass. These parameters permit to define completely the geometry of the celestial bodies involved in the simulation.
- The position of the observer relative to the reference body at each time step.
- The magnetic field and density models attached to the bodies of interest (planet, Sun, planet-star or planet-satellite system, ...). The magnetic field model may be dipolar or of higher order, and the magnetic field lines need to be pre-computed. The density profiles may be that of an ionosphere (exponential decrease with distance from the center of the

body), a stellar corona (decrease in inverse square of the distance from the center), a plasma disk (exponential decreases from both the equatorial plane and the body's center, with different scale heights), or a plasma torus (exponential decrease from the center of a torus of given radius around the body). These parameters enter in the definition of the characteristics of the radio emission, in particular its beaming angle (see section 4).

- The spatial distribution of sources, i.e., the position of the magnetic field lines carrying the current (from their footprint longitude/latitude, their equatorial longitude/distance or their attachment to a satellite) and the frequency range over which the simulation is to be performed.
- The information used to calculate the opening θ of the beaming cone (the distribution function and the energy of the resonating electrons involved in the radio emission, see Section 3) and the thickness $\Delta\theta$ of the beaming conical sheet.

While the source-observer geometry and the magnetic field, plasma density and energy models at the sources are user-defined in ExPRES, the beaming angle θ is self-consistently computed by the code from beaming models described in Section 4 that are based on the CMI theory described in section 3.3. Nevertheless, test simulations may be performed with a predefined beaming angle profile versus frequency (e.g. $\theta(f)$ constant or linearly varying with the frequency).

ExPRES simulations can be adjusted to observations by varying one or several input parameters (e.g., the electrons energy), and the quality (and possibly uniqueness) of the obtained fit permits to derive the value of the corresponding parameter(s) (Hess et al. 2010a).

3. Radiosource locations and characteristics

3.1. Magnetospheric currents

The auroral radio emissions simulated by ExPRES are deeply related to the dynamics of the magnetosphere of magnetized planets. The magnetosphere is the region where the plasma motion is dominated by the magnetic field of the planet. In first approximation, the plasma and the magnetic field are frozen-in. However, the magnetosphere undergoes constraints — both external (solar wind flow) and internal (centrifugal forces, satellite outgassing, ...) — that force the plasma motion relative to the magnetic field. This motion creates an electric field with an associated current, which in turn induces a magnetic field that distorts the magnetic field lines to try to keep them frozen in the plasma. Although this is a crude and over-simplified way to summarize magnetospheric physics, it is as a first approximation sufficient to understand the physics involved in the present paper.

The electric currents follow the magnetic field lines — because the conductivity parallel to the magnetic field is far larger than that perpendicular to it — and close in or above the planet's ionosphere. At some point along the magnetic field line, usually within ~ 1 planetary radius above the ionosphere, the increase in magnetic field strength generates a resistance to the current and thus an electric field parallel to the magnetic field. Electrons accelerated by these electric fields precipitate in the planet's atmosphere and generate auroras. Outside the accelerating region, these electrons move adiabatically, at least in first approximation, so that their parallel velocity v_{\parallel} decreases with the magnetic field strength B :

$$v_{\parallel}^2 = v^2 - \mu B \quad (1)$$

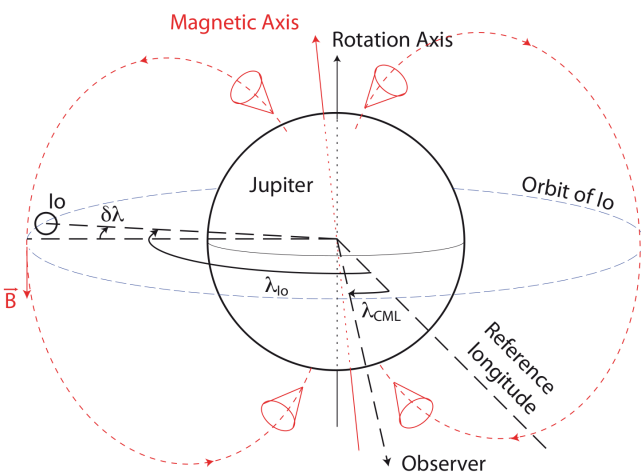


Fig. 2. Examples of the geometry involved in the modeling of the Io-controlled emissions of Jupiter. The emissions depends on the relative position of Io, Jupiter and the observer, in particular on the jovigraphic longitude of the observer (λ_{CML} – Central Meridian Longitude) and that of the active field line which can differ from that of Io λ_{Io} by a lead angle $\delta\lambda$.

with μ the magnetic moment of the electrons. If v_{\parallel} goes to zero before the electrons reach the ionosphere (where they get lost by collisions and power Infrared to Ultraviolet auroras), they are reflected and can participate to the radio emission generation via the CMI.

The three main magnetospheric interactions that lead to electron acceleration are:

- The flow of the solar wind, which deforms the magnetosphere to give it a comet-like shape. This leads to the convection of magnetic field lines from the front to the tail of the magnetosphere, with the generation of one or two convection cells, or to viscous interaction along the magnetospheric border. Along with convection cells, an auroral oval fixed in local time (although modulated by the planet rotation) is formed at the footprints of field lines returning toward the front of the magnetosphere (Dungey 1961). Viscous interactions rather lead to less structured and less stationary auroras, with a strong local time asymmetry (Axford & Hines 1961; Delamere & Bagenal 2010).
- The centrifugal motion of plasma generated inside the magnetosphere. As it moves outward, the conservation of the momentum forces the plasma azimuthal velocity to decrease, in which case it does not corotate anymore with the magnetic field. A current is then generated which re-accelerates the plasma and enforces corotation. This interaction leads to a very stable auroral oval which is fixed in longitude (Cowley & Bunce 2001).
- The interaction of the planetary magnetic field with satellites. When the latter are deeply embedded within the magnetosphere of their parent planet, the plasma that surrounds them (e.g. their ionosphere) is forced to deviate from corotation with the planet's magnetic field. This also generates currents (Neubauer 1980; Saur et al. 2004).

To model this large diversity of interactions and radio auroral counterparts, ExPRES offers several possibilities in the choice of the magnetic field lines which are carrying the radio sources. One can model a full auroral oval, or only part of it (i.e. an auroral arc), either fixed in local time, fixed in longitude (corotating), or in sub-corotation. The position of this oval is defined by a fixed magnetic latitude (i.e. the distance of the field line at the equator). This permits to model auroral radio emissions resulting from solar wind–magnetosphere interactions or from the centrifugal motion of plasma in the magnetosphere, as well as 'hot-spots' related to sub-corotating regions of the magnetosphere (such as those observed at Saturn and modeled using ExPRES in Lamy et al. 2008). Simulations performed in Hess & Zarka (2011) showed the typical morphology of the radio emissions in each of these cases.

ExPRES also permits to impose the active (radio-emitting) field line to be fixed in the frame of a satellite (with a possible longitude shift between the satellite and the active magnetic field line in order to model the propagation time of the current perturbation between the satellite and the planet), thus allowing to simulate satellite–planet interactions (Hess et al. 2008, 2010a; Louis et al. 2017a,b,c). This option may also be used to simulate the interaction between a star and an exoplanet (Hess & Zarka 2011), or interactions between magnetized stars (Kuznetsov et al. 2012, with a model similar to ExPRES).

3.2. Electron acceleration

Besides the distribution of radio sources along specific magnetic field lines, one needs to define the characteristics of the current

system associated to electron acceleration, because they will determine the density and temperature of the electrons inside the radio sources, as well as their distribution function. These characteristics will in turn constrain the beaming pattern of the radio source (see following sections).

The currents created by the interactions described in the previous section are of two types: stationary and transient currents. In these currents, the electrons move in an adiabatic way (in first approximation), thus their parallel velocity v_{\parallel} (respectively perpendicular v_{\perp}) decreases (or increases) with intensity B of the magnetic field. If v_{\parallel} reaches zero before the electrons reach the atmosphere, they reach their mirror point and are then reflected.

For stationary current systems, the magnetic mirroring of high latitude electrons acts as a resistive effect and generates an electric potential gradient along the magnetic field lines. This gradient is usually localized and takes the form of one or several double layers (i.e., discrete potential drops), between the ionosphere and a few radii above it. Between these double layers, the electron density is lower than along the magnetic field lines around (which carry no current) thus forming auroral cavities. In such cavities, the background cold plasma is absent and the electrons are accelerated downwards by potential drops. Thus these accelerated electrons have a horseshoe distribution, resulting from a parallel acceleration followed by pitch angle increase due to the adiabatic motion of the electrons in an increasing magnetic field. Note that at Jupiter, the very low electron density at high latitude does not require the presence of such a cavity. However, the electrons are accelerated to maintain the continuity of the current.

The information about the onset of the interaction propagates along the magnetic field lines at the Alfvén velocity. A transient current system is generated during a time corresponding to at least the travel time at the Alfvén velocity between the interaction site (e.g. the equator in the case of a satellite–magnetosphere interaction) and the planetary ionosphere. Because of the large size of the current system (several planetary radii in this example), this transient phase can last for a long time and may even be longer than the interaction time itself (see e.g. Neubauer 1980; Gurnett & Goertz 1981; Saur et al. 2004, for the Io–Jupiter case).

In this case, electron acceleration is due to the parallel electric field associated to kinetic Alfvén waves above the planet's ionosphere. This electric field is modulated at the Alfvén wave frequency and does not form electric potential drops, and hence does not form directly auroral cavities either (although cavities may slowly build up due to the excitation of ion acoustic waves, Hess et al. 2010a; Matsuda et al. 2012). In this case, the electron density in the current system is the same as outside of it, with the cold component of the plasma remaining present, and the electrons distribution is either a ring or a Kappa-like distribution (Swift 2007; Hess et al. 2007a, 2010b).

3.3. Unstable electron distributions

Wave–particle resonance is reached when the Doppler-shifted pulsation of the wave in the electron's frame ($\omega - k_{\parallel}v_{r_{\parallel}}$) is equal to that of the gyration motion of resonant electrons ($\omega_c\Gamma_r^{-1}$). k_{\parallel} and $v_{r_{\parallel}}$ are respectively the parallel components (to the magnetic field lines) of the wave vector and of the velocity of the resonant particle. $\omega_c = eB/m_e$ is the electron cyclotron pulsation, with B the magnetic field amplitude and e and m_e the electron's charge and mass. Γ_r is the Lorentz factor associated with the resonant electron motion.

The resonance condition thus writes:

$$\omega = \Omega_{c_r} + k_{\parallel} v_{r_{\parallel}} \quad (2)$$

with

$$\Omega_{c_r} = \omega_c \Gamma_r^{-1} = \omega_c \sqrt{1 - v_r^2/c^2} \quad (3)$$

In the weakly relativistic case ($v_r \ll c$), the resonance equation can be rewritten as:

$$v_{r_{\perp}}^2 + \left(v_{r_{\parallel}} - \frac{k_{\parallel} c^2}{\omega_c} \right)^2 = c^2 \left(\frac{k_{\parallel}^2 c^2}{\omega_c^2} + 2 \left(1 - \frac{\omega}{\omega_c} \right) \right) \quad (4)$$

Thus the resonance equation is that of a circle in the $[v_{\parallel}, v_{\perp}]$ velocity space, whose center v_0 , located on the v_{\parallel} axis, is given by:

$$v_0 = \frac{k_{\parallel} c^2}{\omega_c} \quad (5)$$

which can be rewritten as:

$$v_0 = \frac{\omega}{\omega_c} c N \cos \theta \quad (6)$$

where θ is the direction of the emission ($k \cos \theta = \mathbf{k} \cdot \mathbf{b} = k_{\parallel}$) and $N = ck/\omega$ is the refractive index value (which must be taken into account to reproduce the observations, as shown by Ray & Hess 2008).

The resonance condition can thus be rewritten as:

$$\omega = \Omega_{c_r} + k_{\parallel} v_{r_{\parallel}} = \Omega_{c_r} \left(1 - \frac{v_{r_{\parallel}}}{c} N \cos \theta \right)^{-1} \quad (7)$$

Therefore, the resonance condition does not only define the pulsation of the amplified wave ω , but also the direction of the emission θ .

The resonance equation is under-constrained as there are two variables (ω and θ) to determine for a single equation. To solve it one must consider another constrain brought by the CMI amplification equation, which states that the amplification occurs for positive gradients of the electron perpendicular velocity distribution around the resonant velocities v_r (Wu 1985). Given an electron distribution, it is possible to determine which sphere has the maximum positive gradients along its border and then to determine the angle of emission θ . Then the resonance equation gives the emission frequency f . Subsequently, we will indifferently call 'frequency' the frequency f or the pulsation ω , since $\omega = 2\pi f$.

Unstable electron distributions are common in the auroral regions. They may be so-called horseshoe distributions as that shown on Figure 3, or ring distributions which are incomplete horseshoes with a limited pitch angle spread of the electron velocity (Su et al. 2008). These distributions may fulfill various resonance conditions, the two main ones being the oblique wave resonance (corresponding to $v_0 \neq 0$ and generically called loss-cone-driven) and the perpendicular wave resonance (corresponding to $v_0 = 0$ and generically called 'shell-driven') (Wu 1985; Hess et al. 2007a). The oblique mode resonance circle lies inside the loss-cone of the electron distribution and is tangent to it, where the distribution gradient generates the largest amplification rate, whereas the perpendicular mode resonance circle is tangent to the inner edge of the shell. These two resonance circles are shown by dashed lines on Figure 3.

These modes differ by the frequency of the emission, deduced from the resonance equation (Eq. 7). The perpendicular

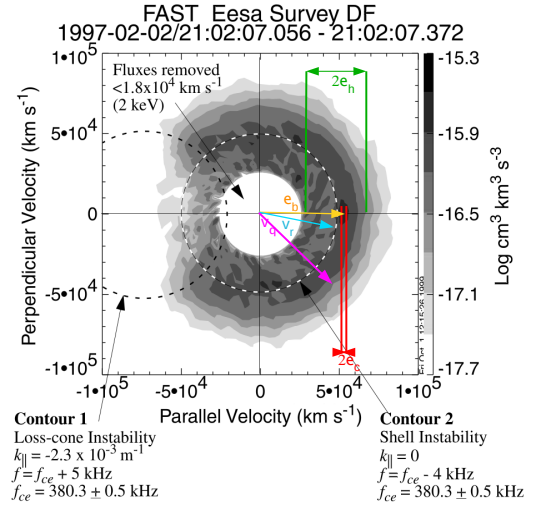


Fig. 3. An unstable electron distribution measured by FAST in the Earth auroral region (Ergun et al. 2000). This kind of distribution is typical in the auroral regions emitting radio emissions, it consists in a cold (a few eV) Gaussian distribution with a warmer (a few 100's eV) halo which is shifted in energy by a few keV and which pitch angle is scattered due to magnetic mirroring. We assumed a distribution function of that kind in our modeling of the beaming angle from auroral cavities. Velocity dispersion corresponding to the cold and halo temperature (ϵ_c and ϵ_h) and the velocity shift corresponding to the beam energy (ϵ_b) are shown. The resonant electron velocity (v_r) and the equivalent "thermal" velocity (v_θ) are shown too.

emission frequency is obtained using $v_{r_{\parallel}} = 0$ and is always smaller than the cold electron cyclotron frequency:

$$\omega_{shell} = \Omega_{c_r} < \omega_c \quad (8)$$

The emission frequency of the oblique mode is obtained from the center of the circle tangent to the loss-cone boundary at a point that can be obtained through elementary trigonometry and Eqs. 6 and 7 (Wu 1985; Hess et al. 2008):

$$v_0 = v_r / \cos \alpha \Rightarrow \omega_{lc} \approx \omega_c \Gamma_r > \omega_c \quad (9)$$

where α is the resonant electrons pitch angle (i.e. the loss-cone angle), which depends on frequency:

$$\cos \alpha = v_{r_{\parallel}} / v_r = (1 - \omega_c / \omega_{c_{\max}})^{-1/2} \quad (10)$$

with $\omega_{c_{\max}}$ the electron cyclotron frequency at the altitude below which the electrons are lost by collision with the planetary atmosphere.

Contrarily to perpendicular emission, oblique emission is emitted above the cold plasma electron cyclotron frequency. The difference in frequency between these modes has important consequences due to the characteristics of the dispersion relation of the right-handed waves in the plasma (Lassen 1926).

While the bulk electron velocity is zero in the plasma rest frame, the velocity of individual electron is not zero. One thus needs to introduce in the refraction index expression a Lorentz factor Γ_{th} , translating the non-zero velocity of the electrons in the plasma rest frame (Pritchett 1984; Louarn & Le Quéau 1996b). Exact computation of this relativistic correction may be complicated (Pritchett 1984), but it can be estimated by introducing an equivalent 'thermal' velocity v_{th} , so that the mean energy of the electrons in the plasma rest frame is $m_e v_{th}^2 / 2$ (Louarn & Le Quéau 1996b; Mottez et al. 2010). This relativistic term is of importance, as it participates — along with the ratio between the

plasma and the electron cyclotron frequency (ω_p/ω_c) — in the determination of the mode(s) on which the waves can be emitted (or not).

Thus, in a non-zero temperature plasma, the expression of the refraction index is:

$$N^2 = 1 - \frac{\omega_p^2}{\omega^2 - \frac{\Omega_{c_{th}}^2 \sin^2 \theta}{2(1-\omega_p^2/\omega^2)} \left(1 + \sqrt{1 + \left(\frac{2\omega(1-\frac{\omega_p^2}{\omega^2}) \cos \theta}{\Omega_{c_{th}} \sin^2 \theta} \right)^2} \right)} \quad (11)$$

$$\Omega_{c_{th}} = \omega_c \Gamma_{th}^{-1} = \omega_c \sqrt{1 - v_{th}^2/c^2} \quad (12)$$

From Equation 11 one sees that a cutoff frequency ($N=0$) exists for Right-Handed (RH) modes. Below this frequency, the wave is on the Right-Extraordinary R-Z mode, and above it, the wave is on the Right-Extraordinary R-X mode. Only the R-X mode connects to the $\omega = ck$ dispersion relation of freely propagating radio waves, whereas the R-Z mode is trapped inside its source region (see Figure 4a). Hence, R-X mode waves are the only RH waves observed as radio emissions (Louarn & Le Quéau 1996a). The 'choice' of the CMI between the R-Z and R-X modes is determined by two factors: the wave pulsation ω , which is constrained by the resonant electron velocity, and the cutoff frequency, which depends on ω_p/ω_c and v_{th} . In the auroral regions the cutoff frequency is always within a few percent of ω_c . Lower values of ω_p/ω_c and/or higher values of v_{th} lead to smaller values of the cutoff frequency — that can even lie below ω_c —, whereas higher ω_p/ω_c and/or lower v_{th} lead to larger cutoff frequencies.

ExPRES computes the cutoff frequency at each point of the user-defined radio source from Eq. 11, and the wave frequency from the electron velocity distribution (see section 3.3), and considers that emission is produced only if the wave frequency is above the cutoff frequency. Thus ExPRES needs to be fed with the local magnetic field strength (that defines ω_c), the local plasma density (that defines ω_p), and the mean energy of the electrons in the source (that defines v_{th}).

Note that the modes discussed above all have pure circular polarization. Elliptically polarized waves amplified by the CMI can split in L-O and R-X modes on index gradients (Melrose 1980; Shaposhnikov et al. 1997; Louarn & Le Quéau 1996a). However, in the following we will only consider R-X emissions, because they are the dominant ones in most auroral emissions observed, and for that reason they are the only ones simulated by the ExPRES code so far.

4. Radiation pattern

4.1. Transient (Alfvénic) current system

In the case of a transient current system, electrons are accelerated by Alfvén waves electric fields and a ring (Hess et al. 2007a) or a Kappa-like (Swift 2007) distribution forms. Also, the Alfvén waves do not generate a deep auroral cavity devoid of cold plasma (Mottez et al. 2010). In these conditions, the oblique R-X mode is the one that will be favoured. Its beaming angle is obtained by solving together equations 11, 6 and 9. First, the refraction index is obtained by equating the value of the center of the resonance sphere v_0 in Eqs. 6 and 9:

$$N = \frac{\Gamma_r^{-1} v_r}{\cos \alpha} \frac{1}{c \cos \theta} = \frac{\chi}{\cos \theta} \quad (13)$$

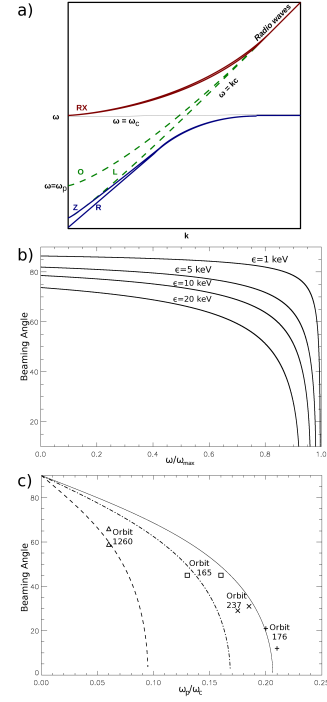


Fig. 4. a) Sketch of the dispersion relation of the electromagnetic waves in a plasma, following the Appleton-Hartree equation. Only R-X and L-O modes can escape the plasma and become radio waves. b) Beaming angle of the oblique emissions as a function of the ratio of the emission frequency to the surface electron cyclotron frequency, for different values of the electrons energy and $N = 1$. c) Beaming angle of the perpendicular emissions as a function of ω_p/ω_c outside of a cavity. Symbols correspond to AKR beaming angle measurements by Louarn & Le Quéau (1996a). Lines are theoretical beaming angles computed using Eqs. 18 & 23, constrained by density measurements of Louarn & Le Quéau (1996a) for orbit 176 (solid line), orbit 1260 (dashed) and orbit 165 (dot-dashed).

The dispersion relation is obtained from the dielectric tensor (Stix 1962) and can be written as:

$$AN^4 - BN^2 + C = A\chi^4 - B\chi^2 \cos^2 \Theta + C \cos^4 \Theta = 0 \quad (14)$$

Setting $v_p = \omega_p^2/\omega_c^2$ and using the resonance equation (Eq. 7) and the notation of Stix (1962):

$$S = 1 - \frac{2v_p c^2}{v_r^2 + v_{th}^2}; P = 1 - \frac{2v_p c^2}{2c^2 + v_r^2}; D = v_p \frac{2c^2 - v_r^2}{v_r^2 + v_{th}^2} \quad (15)$$

the coefficients of Eq. 14 can be rewritten to obtain a second order equation in $\cos^2 \theta$:

$$S\chi^4 + \left[\chi^4(P - S) - \chi^2(PS + S^2 - D^2) \right] \cos^2 \theta + \left[P(S^2 - D^2) - \chi^2(PS - S^2 + D^2) \right] \cos^4 \theta = a \cos^4 \theta + b \cos^2 \theta + c = 0 \quad (16)$$

The solution for the R-X mode is:

$$\cos^2 \theta = \frac{-b + \sqrt{b^2 - 4ac}}{2a} \quad (17)$$

For a transient current system, the beaming angle inside the source computed by ExPRES is the exact solution of the above

equation. To perform the calculation, ExPRES needs the user to specify the accelerated electron mean energy (v_r^2) and the plasma temperature (v_{th}^2), whereas the ratio between plasma frequency and electron cyclotron frequency is deduced from the density profiles associated with the celestial bodies considered (see section 2).

Panel b of Figure 4 shows the evolution of the beaming angle as a function of the ratio between the emission frequency ω and the maximal cyclotron frequency reachable $\omega_{c_{max}}$ for different resonant electron energies ϵ . The plasma frequency was considered to be negligible, so that $N = 1$ in that case.

4.2. Steady-state current system

4.2.1. Refraction in the source

At the source, the beaming of the radio emissions generated by a steady-state current system is more simple than in the previous case: if the R–X mode can be amplified, waves are beamed perpendicular to the magnetic field. However the emission is most of the time observed to be generated inside of a plasma cavity and to be refracted on its border (Louarn & Le Quéau 1996a,b). This leads to a very complex situation due to the fact that the beaming angle outside the cavity depends on the cavity profile. There is a wide variety of possible cavity profiles and very few constraints on them. Moreover, depending on the shape of the cavity, waves can be partially trapped and resonate inside the cavity, with an impact on the radio beaming. As a consequence, it is not possible to define an exact general solution to the problem of the beaming angle of a radio source inside a cavity. Even for a well-defined cavity profile, computation of the beaming requires a ray-tracing algorithm, which needs too much computational power to be integrated in ExPRES.

ExPRES thus uses an approximate solution, assuming that the refraction mainly occurs inside the cavity and not on its borders. The need for refraction inside the source was already emphasized by Louarn & Le Quéau (1996b), and its existence is related to the presence of a gradient of refraction index inside the cavity due to the gradient of magnetic field strength. This gradient is mainly parallel to the magnetic field. Thus, the major difference between ExPRES computation and reality is that ExPRES assumes that the wave reaches a region where the refraction index is $N = 1$ inside the source, in which case refraction on the cavity border has a low impact on the final beaming angle, whereas in reality a slight increase of the refraction index in the cavity allows the wave to escape it, so that a large part of the refraction takes place on the cavity border. Note that the assumption made in ExPRES is likely to be a good approximation in the case of a large cavity (in terms of its perpendicular size relative to the radio wavelength), because in that case a significant fraction of the refraction is indeed expected to take place inside the cavity. In such a large cavity, strong trapping of the wave is also unlikely, and thus no effect is expected on the radio beaming. It is also well suited for cases in which hot plasma is observed out of cavities (generally at very high latitude) such as in the case of the Saturn SKR source crossing (Lamy et al. 2010, 2011).

Under the above assumption, assuming that the index gradient is parallel to the magnetic field and using Snell–Descartes law, computation of the radio beaming angle simply becomes:

$$\sin \theta = N \quad (18)$$

with the refraction index N being that of a pure X mode (purely perpendicular to the magnetic field) with $\omega = \Omega_{c_r}$, i.e.:

$$N^2 = 1 - \frac{\omega_{p_{source}}^2 \left(1 - \frac{\omega_{p_{source}}^2}{\Omega_{c_r}^2}\right)}{\Omega_{c_r}^2 - \Omega_{c_{th}}^2 - \omega_{p_{source}}^2} \quad (19)$$

It appears clearly from this equation that in order to have a real refraction index (permitting wave propagation), the electron mean energy (i.e. 'temperature') must be larger than the resonant electron mean energy so that $\Gamma_{th} > \Gamma_r$ and thus $\Omega_{c_r}^2 - \Omega_{c_{th}}^2 > 0$.

4.2.2. Electron distribution model

Equation 19 is very sensitive to the variation of each parameter, and thus the relation between them has to be set very carefully from physical considerations relevant to the source considered. This is particularly the case for the electron distribution.

ExPRES models the unstable distribution as a bi-Maxwellian distribution at rest accelerated to a given energy. Thus, we define three characteristic electron energies: the beam energy (ϵ_b) which corresponds to the energy of accelerated electrons (usually several keV), the electron's core thermal energy (ϵ_c) which is the temperature of the core of the distribution of the background electrons (usually a few eV to a few tens of eV), and the electron's halo temperature (ϵ_h) which is the mean energy of supra-thermal electrons (usually a few hundreds of eV). The electron density inside the source is taken proportional to that outside of the source (i.e., that of the plasma before acceleration), with a proportionality coefficient deduced from current conservation (density \times velocity is constant). The plasma frequency in the source is thus deduced from the ratio between beam and core energies:

$$\omega_{p_{source}}^2 = \sqrt{\frac{\epsilon_c}{\epsilon_b}} \omega_p^2 = \eta \omega_p^2 \quad (20)$$

The halo temperature is used to determine the resonant electron energy. This energy is not that of the beam, because the resonance circle of a shell driven CMI passes through the region of largest $\nabla_{v_{r\perp}} f(\mathbf{v}_r)$, i.e., within the inner edge of the shell and not along the peak of the distribution. For a shifted-Maxwellian distribution of the energies in the beam (with a standard-deviation ϵ_h), the largest positive gradient is obtained for an energy $\epsilon_b - \epsilon_h$. Thus the difference between the electron's mean and resonant energies is :

$$v_{th}^2 - v_r^2 = \frac{2\epsilon_h}{m_e} \quad (21)$$

As noted in Mottez et al. (2010), using ϵ_c instead of ϵ_h would not permit the generation of an X–mode wave (the plasma needs to be 'hot'), hence our assumption of the presence of a halo, which is usually observed at energies of a few hundreds eV in magnetospheric plasmas (cf. Figure 3 and Ergun et al. 2000).

Depending on what the user knows as physical parameters, two choices are possible with ExPRES. Either the user specifies the plasma density in the source $\omega_{p_{source}}$, or it only gives the global magnetospheric density (not directly that of the sources).

In the first case (if the user knows $\omega_{p_{source}}$), using Equations 12 and 21, the refraction index of Equation 19 becomes:

$$N^2 = 1 + \frac{1 - \frac{\omega_{p_{source}}^2}{\Omega_{c_r}^2}}{1 - \frac{\omega_c^2}{\omega_{p_{source}}^2} \frac{2\epsilon_h}{m_e c^2}} \quad (22)$$

In the second case (if the user does not know $\omega_{p_{source}}$), using Equation 20 the refraction index of Equation 19 then becomes:

$$N^2 = 1 + \frac{1 - \eta v_p \Gamma_r^2}{1 - \frac{2\epsilon_h}{\eta v_p m_e c^2}} < 1 \text{ (R-X mode)} \quad (23)$$

Figure 4-c displays the beaming angles computed using the above equation, with parameters η and ϵ_h deduced from measurements in Terrestrial auroral cavities. η was estimated from the densities inside ($\sim 1 \text{ cm}^{-3}$) and outside (deduced from measured f_{pe}) of the cavities (Louarn & Le Quéau 1996a), and ϵ_h was taken $\approx 900 \text{ eV}$, consistent with the distributions measured by Ergun et al. (2000). With measured beam energies $\epsilon_b = 3 - 10 \text{ keV}$, the electrons' resonant energy is about 2–9 keV. The modeled beaming curves are in good agreement with the observed values of the beaming angles (symbols) for the observations of Auroral Kilometer Radiation corresponding to the density measurements in (Louarn & Le Quéau 1996a).

4.3. Refraction in the source vicinity

The refraction index has an important effect inside the source since the resonance process occurs close to the X mode cutoff frequency, where the refraction index varies rapidly for small variation of the plasma parameters.

Outside of the source, the refraction index rapidly goes to 1, in which case the waves escape freely as radio waves, or to 0, in which case the waves meet a reflection layer and are reflected. This phenomenon may happen close to the source, where the local cyclotron frequency is still close to that inside the source (and thus close to the wave frequency), or far from it — for example radio emissions from auroral region may be refracted in the equatorial plasma sheet. ExPRES only takes into account the former case, i.e. refraction in the source vicinity, because it does not include any ray-tracing algorithm.

This refraction effect outside the source differs from that inside the source by the fact that it is not symmetrical relative to the magnetic field vector. The ExPRES code models it under the approximation of planar refraction index iso-surfaces at each point of the wave propagation, with a refraction index varying only in the local meridian plane. Thus the gradient of refraction index is assumed to be null in the longitudinal direction, so that the normal to the refraction index planes has a null longitudinal component. The modification of the beaming angle is then obtained easily from the Snell–Descartes law.

5. Simulation results, Conclusions and Perspectives

5.1. Versions of ExPRES

Each version of the code has seen new modules added and minor bugs fixed. Here is given a summary of the major evolutions.

The first versions (0.1, 0.2 and 0.3) of the ExPRES code were developed to predict and interpret the future observations of the NASA *Juno* space mission to Jupiter. Indeed, unlike previous low frequency radio astronomy experiments (such as Cassini/RPWS, Gurnett et al. 2004), which were able to measure the 4 Stokes parameters and the \mathbf{k} vector of incoming waves (Cecconi et al. 2009), the radio experiment onboard *Juno* (Matousek 2007; Bagenal et al. 2017), named Waves (Kurth et al. 2017), only measures the total intensity of incoming radio waves versus time and frequency (it also performs some limited direction-finding, but that proved effective for case studies Imai

et al. 2017). The development of the ExPRES tool was therefore necessary to determine the origin of the emissions.

Version 0.4 of the code allowed a generalization to Saturn and version 0.5 to exoplanets. For version 0.6, the code architecture was completely redesigned and the production of 3D movies was added. The current stable version is 1.0 and allows, from JSON formatted (Bray 2017) input files, to produce the simulation results in CDF (Space Physics Data Facility 2018).

5.2. Output parameters

Different output parameters can be selected. The default setup returns the following information at each time and frequency step:

- **Polarization**: polarization of the observed wave (if it is detected), making it possible to differentiate emission from the northern (<0) or the southern hemisphere (>0);
- **Theta**: opening of the conical emission sheet;
- **CML**: longitude of the observer;
- **ObsLatitude**: planetocentric latitude of the observer;
- **ObsDistance**: distance (in planetary radius) between the observer and the planet;
- **SrcFreqMax**: maximum frequency on the active flux tube at each time step;
- **Fp**: electronic plasma frequency in the sources;
- **Fc**: electronic cyclotron frequency in the sources.

Additional information may be requested by the user, such as:

- the azimuth ϕ of the wave seen by the observer, i.e., the part of the conical emission sheet from which the wave seen by the observer comes from, with the reference $\phi = 180^\circ$ the direction of the wave towards the magnetic equator;
- the equatorial longitude of the sources. For simulations of emissions induced by a moon, the longitude of the sources is the longitude of the moon;
- the position (x, y, z) of the sources;
- the local time of the observer (under development).

5.3. Simulation results

Figure 5 shows an observations with the Nançay Decameter Array (NDA) of the Io-controlled Jovian emissions on January 21st, 2013. The two panels respectively correspond to the right-handed and left-handed emissions. This observation is dominated by an Io–B emission (emitted from a northern–dawn source, see Fig. 2) that is mostly right-handed (consistent with its northern hemisphere origin), but a fainter Io–D left-handed-polarized emission (thus emitted from a southern–dawn source) is also visible later. These emissions can be modeled using ExPRES. The simulated dynamic spectra are overplotted in red on top of the NDA data. The simulations matching best the observations are obtained assuming emissions from magnetic field line connected to the Io Main Alfvén Wing footprint, using the JRM09 magnetic field model (Connerney et al. 2018) and electrons with energies of 2.5 keV (in the northern hemisphere) and 3.5 keV (in the southern hemisphere).

ExPRES has already been used to model observations, attempting to reproduce the time–frequency morphology of the radio emissions from Jupiter (Hess et al. 2008, 2011, 2010a; Ray & Hess 2008) and Saturn (Lamy et al. 2008, 2011, 2013). It allowed these authors to determine the localization of the Io–Jupiter current circuit (downstream of the instantaneous Io–Jupiter field line) and to discover subcorotating field-aligned current systems at Saturn. These works also allowed them to put

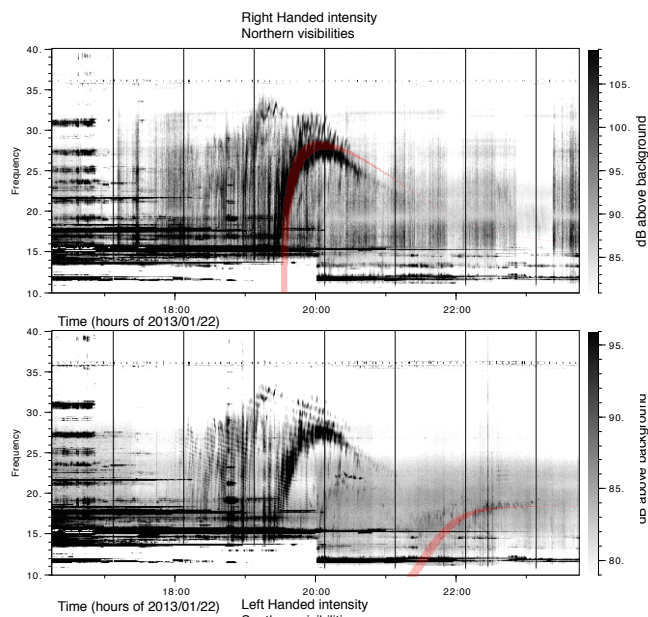


Fig. 5. Example of radio emissions (Io-controlled Jovian emissions) modeling using ExPRES overlapped on dynamic spectra observed by the Nançay Decameter Array. The observation was performed on January 21st, 2013. Right-handed (top) and left-handed (bottom) polarization are separated. The observed emission (bright one in the northern hemisphere and dimmer one in the southern hemisphere) are well modeled by ExPRES (in red), assuming a source originating from the magnetic field line connected to the main Io Alfvén wing spot on Jupiter computed using the JRM09 model (Connerney et al. 2018), and electrons with energies (ϵ_e) of 2.5 keV (North) and 3.5 keV (South).

constraints on the energy of the accelerated electrons involved in the auroral radio components at these planets. Electrons energies of the order of a few keV were found at Jupiter and a few tens of keV at Saturn, consistent with UV observations.

ExPRES has also been used to predict and interpret radio emission from Jupiter, using a predefined dataset for the input parameters (based on a parametric study, see Louis et al. 2017b). It allowed the authors to detect radio emissions induced by Europa and Ganymede (Louis et al. 2017a) and interpret the time-frequency morphology of *Juno*/Waves observations (Louis et al. 2017c), which was the initial goal of the code.

ExPRES was similarly used to simulate the radio environment of the Jupiter Icy Moon Explorer (JUICE) spacecraft planned to be sent to Jupiter by ESA, in order to estimate to what extent natural radio emissions from Jupiter’s magnetosphere below 40 MHz would pollute the spacecraft radar measurements in the range 5–50 MHz (Ceconi et al. 2012).

Finally, Hess & Zarka (2011) studied the type of information that can be deduced, using ExPRES, from the morphology of the radio emissions — still to be discovered — from exoplanetary magnetospheres or star-planet systems involving plasma or magnetic interactions. These information include the magnetic-field strength and the rotation period of the emitting body (planet or star), the orbital period, the orbit’s inclination, and the magnetic field tilt relative to the rotation axis or offset relative to the center of the planet. For most of these parameters, radio observations provide an unique mean of measuring them.

5.4. Accessibility

The ExPRES code is written in IDL¹. The code is available under MIT licence on GitHub within the MASER² library repository: <https://github.com/maserlib/ExPRES>. The current version of the ExPRES code (V1.0) has been validated using IDL version 8.4.

Precomputed ExPRES simulation runs are available through different interfaces described on the MASER project (Ceconi et al. 2018a,b) website³: (i) a web directory listing access; (ii) a virtual observatory access using the EPN-TAP (Erard et al. 2018); and (iii) a streaming access using the das2 server framework (Piker 2017) through the MASER das2 Server. Table 1 provides URLs for all access interfaces.

The ExPRES code is also available for run-on-demand operations at <https://voparis-uws-maser.obspm.fr>. This computing interface requires an ExPRES JSON input configuration file. Examples of such configuration files are available through the web directory listing or virtual observatory catalog: each of the precomputed file is provided with its input configuration file. The JSON input files must conform to the corresponding JSON-scheme specification, the current version of which is available at <https://voparis-ns.obspm.fr/maser/expres/v1.0/schema#>.

5.5. Perspectives

ExPRES has proved to be a very useful tool for the modeling, analysis and interpretation of planetary radio emissions, the preparation and operation of planetary missions, as well as for the interpretation of the to-be-detected radio emissions from exoplanets. Such detections are expected soon as a result of extensive observing programs with giant radio telescopes such as LOFAR, UTR2, GMRT, NenuFAR and ultimately SKA.

Future uses will include the modeling of the time-frequency morphology of Jovian hectometer and broadband kilometer emissions (Boischoit et al. 1981), the modeling of the longitude-frequency morphology of Jovian hectometer and Io-independent decameter emissions (Imai et al. 2008, 2011), the search for induced radio emission of kronian satellite or the search for radio emission of Uranus and Neptune. Future developments may include a more quantitative treatment of the simulated emission intensity.

Acknowledgments

Version 0.1 to 0.5 of ExPRES have been developed as SERPE ("Simulateur d’Émissions Radio Planétaires et Exoplanétaires") by the LESIA laboratory under Observatoire de Paris and CNRS funding. Version 0.6.0 was developed by S. L. G. Hess on his own resources and with support from the LESIA, Observatoire de Paris for the online services. Later versions, including the current 1.0.0 version, were developed by the MASER team (<http://maser.lesia.obspm.fr>) which gathers personnel and funding from CNRS, CNES and Observatoire de Paris. Technical support from PADC (Paris Astronomical Data Center) is also acknowledged, with the very helpful contribution of P. Le Sidaner (DIO, Observatoire de Paris) and M. Servil-

¹ Interactive Data Language, Exelis Visual Information Solutions, Boulder, Colorado

² Measuring, Analyzing and Simulating Emissions in the Radio range

³ ExPRES page on the MASER website: <http://maser.lesia.obspm.fr/tools-services-6/expres>

Description	Interface	Access URL	Client
Web directory listing	HTTP	http://maser.obspm.fr/data/serpe/	Web Browser
Virtual Observatory dataset catalog	EPN-TAP	http://voparis-tap-maser.obspm.fr:80/tableinfo/expres.epn_core	VESPA or TAP client (Erard et al. 2018)
Streaming access	Das2	http://voparis-maser-das.obspm.fr/das2/server	Autplot (Faden et al. 2010)

Table 1. List of access interfaces for ExPRES precomputed dataset

lat (LUTH, Observatoire de Paris). The Nançay Decameter Array acknowledges the support from the Programme National de Planétologie and the Programme National Soleil–Terre of CNRS–INSU. S. L. G. Hess thanks the MOP team of the LASP (Colorado Univ. Boulder) and R. Modolo (LATMOS/CNRS) for scientific support and fruitful comments. Part of the data distribution setup has been done in the frame of the Europlanet H2020 Research Infrastructure project, which has received funding from the European Union’s Horizon 2020 research and innovation programme under grant agreement No 654208.

References

- Axford, W. I. & Hines, C. O. 1961, *Canadian Journal of Physics*, 39, 1433
- Bagenal, F., Adriani, A., Allegrini, F., et al. 2017, *Space Science Reviews*, 213, 219
- Boischoit, A., Lecacheux, A., Kaiser, M. L., et al. 1981, *J. Geophys. Res.*, 86, 8213
- Bray, T. 2017, *The JavaScript Object Notation (JSON) Data Interchange Format*, Tech. Rep. RFC 8259, IETF
- Cecconi, B., Hess, S., Hérique, A., et al. 2012, *Planet. Space Sci.*, 61, 32
- Cecconi, B., Lamy, L., Zarka, P., et al. 2009, *Journal of Geophysical Research (Space Physics)*, 114, A03215
- Cecconi, B., Le Sidaner, P., Savalle, R., et al. 2018a, in *PV-2018 Conference Proceedings*, 20–24
- Cecconi, B., Loh, A., Le Sidaner, P., et al. 2018b, *Earth and Space Science Open Archive* [<https://www.essoar.org/doi/pdf/10.1002/essoar.10500145.1>]
- Connerney, J. E. P., Kotsiaros, S., Oliverson, R. J., et al. 2018, *Geophysical Research Letters*, 45, 2590
- Cowley, S. W. H. & Bunce, E. J. 2001, *Planetary and Space Science*, 49, 1067
- Delamere, P. A. & Bagenal, F. 2010, *Journal of Geophysical Research (Space Physics)*, 115, 10201
- Dungey, J. W. 1961, *Physical Review Letters*, 6, 47
- Erard, S., Cecconi, B., Le Sidaner, P., et al. 2018, *Planet. Space Sci.*, 150, 65
- Ergun, R. E., Carlson, C. W., McFadden, J. P., et al. 2000, *ApJ*, 538, 456
- Faden, J., Weigel, R. S., Merka, J., & Friedel, R. H. W. 2010, *Earth Sci. Inform.*, 3, 41
- Genova, F. & Aubier, M. G. 1985, *Astron. and Astrophys.*, 150, 139
- Gurnett, D. A. & Goertz, C. K. 1981, *Journal of Geophysical Research (Space Physics)*, 86, 717
- Gurnett, D. A., Kurth, W. S., Kirchner, D. L., et al. 2004, *Space Sci. Rev.*, 114, 395
- Hess, S., Cecconi, B., & Zarka, P. 2008, *Geophys. Res. Lett.*, 35, 13107
- Hess, S., Mottez, F., & Zarka, P. 2007a, *J. Geophys. Res.*, 112, A11212
- Hess, S., Pétrin, A., Zarka, P., Bonfond, B., & Cecconi, B. 2010a, *Planetary and Space Sciences*, 58, 1188
- Hess, S., Zarka, P., & Mottez, F. 2007b, *Planetary and Space Science*, 55, 89
- Hess, S. L. G., Bonfond, B., Zarka, P., & Grodent, D. 2011, *J. Geophys. Res.*, 116, A05217
- Hess, S. L. G., Delamere, P., Dols, V., Bonfond, B., & Swift, D. 2010b, *Journal of Geophysical Research (Space Physics)*, 115, 6205
- Hess, S. L. G., Echer, E., Zarka, P., Lamy, L., & Delamere, P. A. 2014, *Planet. Space Sci.*, 99, 136
- Hess, S. L. G. & Zarka, P. 2011, *Astron. and Astrophys.*, 531, A29
- Imai, M., Imai, K., Higgins, C. A., & Thieman, J. R. 2008, *Geophys. Res. Lett.*, 35, 17103
- Imai, M., Imai, K., Higgins, C. A., & Thieman, J. R. 2011, *Journal of Geophysical Research (Space Physics)*, 116, 12233
- Imai, M., Kurth, W. S., Hospodarsky, G. B., et al. 2017, *Geophysical Research Letters*, 44, 6508
- Kaiser, M. L., Zarka, P., Kurth, W. S., Hospodarsky, G. B., & Gurnett, D. A. 2000, *J. Geophys. Res.*, 105, 16053
- Kurth, W. S., Hospodarsky, G. B., Kirchner, D. L., et al. 2017, *Space Science Reviews*, 213, 347
- Kuznetsov, A. A., Doyle, J. G., Yu, S., et al. 2012, *ApJ*, 746, 99
- Lamy, L., Cecconi, B., Zarka, P., et al. 2011, *Journal of Geophysical Research (Space Physics)*, 116, A04212
- Lamy, L., Prangé, R., Pryor, W., et al. 2013, *Journal of Geophysical Research (Space Physics)*, 118, 4817
- Lamy, L., Schippers, P., Zarka, P., et al. 2010, *Geophys. Res. Lett.*, 37, L12104
- Lamy, L., Zarka, P., Cecconi, B., Hess, S., & Prangé, R. 2008, *Journal of Geophysical Research (Space Physics)*, 113, 10213
- Lamy, L., Zarka, P., Cecconi, B., et al. 2018, *Science*, 362, aat2027
- Lassen, H. 1926, *I. Zeitschrift für Hochfrequenztechnik*, 28, 109
- Lecacheux, A., Boudjada, M. Y., Rucker, H. O., et al. 1998, *A&A*, 329, 776
- Louarn, P. 1992, *Advances in Space Research*, 12, 121
- Louarn, P., Allegrini, F., McComas, D. J., et al. 2017, *Geophysical Research Letters*, 44, 4439
- Louarn, P. & Le Quéau, D. 1996a, *Planet. Space Sci.*, 44, 199
- Louarn, P. & Le Quéau, D. 1996b, *Planet. Space Sci.*, 44, 211
- Louis, C. K., Lamy, L., Zarka, P., Cecconi, B., & Hess, S. L. G. 2017a, *Journal of Geophysical Research (Space Physics)*, 122, 9228
- Louis, C. K., Lamy, L., Zarka, P., et al. 2017b, in *Planetary Radio Emissions VIII*, edited by G. Fisher et al., Austrian Academy of Sciences Press, Vienna, 59–72
- Louis, C. K., Lamy, L., Zarka, P., et al. 2017c, *Geophysical Research Letters*, 44, 9225
- Matousek, S. 2007, *Acta Astronautica*, 61, 932
- Matsuda, K., Terada, N., Katoh, Y., & Misawa, H. 2012, *Journal of Geophysical Research (Space Physics)*, 117, 10214
- Melrose, D. B. 1980, *Plasma Astrophysics (Gordon and Breach, New York)*
- Mottez, F., Hess, S., & Zarka, P. 2010, *Planet. Space Sci.*, 58, 1414
- Neubauer, F. M. 1980, *J. Geophys. Res.*, 85, 1171
- Piker, C. 2017, *Das2 Version 2.2.2 Interface Reference*, Tech. rep., University of Iowa
- Pottelette, R. & Pickett, J. 2007, *Nonlinear Processes in Geophysics*, 14, 735
- Pritchett, P. L. 1984, *J. Geophys. Res.*, 89, 8957
- Queinnee, J. & Zarka, P. 1998, *J. Geophys. Res.*, 103, 26649
- Ray, L. C. & Hess, S. 2008, *J. Geophys. Res.*, 113, A11218
- Saur, J., Neubauer, F. M., Connerney, J. E. P., Zarka, P., & Kivelson, M. G. 2004, *Plasma interaction of Io with its plasma torus (Jupiter. The Planet, Satellites and Magnetosphere)*, 537–560
- Shaposhnikov, V. E., Kocharovsky, V. V., Kocharovsky, V. V., et al. 1997, *Astron. and Astrophys.*, 326, 386
- Space Physics Data Facility. 2018, *Common Data Format, NASA-GSFC, version 3.7.0*
- Stix, T. H. 1962, *The Theory of Plasma Waves (McGraw-Hill, New York)*
- Su, Y.-J., Ma, L., Ergun, R. E., Pritchett, P. L., & Carlson, C. W. 2008, *Journal of Geophysical Research (Space Physics)*, 113, 8214
- Swift, D. W. 2007, *Journal of Geophysical Research (Space Physics)*, 112, 12207
- Treumann, R. A. 2006, *Astron. and Astrophys. Review*, 13, 229
- Wu, C. S. 1985, *Space Science Reviews*, 41, 215
- Zarka, P. 1998, *J. Geophys. Res.*, 103, 20159
- Zarka, P. 2004, *Advances in Space Research*, 33, 2045